Domain wall dynamics in $(Co/Ni)_n$ nanowire with anisotropy energy gradient for neuromorphic computing applications

William Wai Lum Mah, Durgesh Kumar, Tianli Jin, S.N. Piramanayagam*

School of Physical and Mathematical Sciences, Nanyang Technological University, 21, Nanyang Link, Singapore 637371, Singapore

*prem@ntu.edu.sg

Abstract

Artificial Intelligence (AI) has been gaining traction recently. However, they are executed on devices with the von Neumann architecture, requiring high power input. Consequently, brain-inspired neuromorphic computing has been gaining attention because it is expected to be more power efficient and be more suitable for AI. Designing of NC circuits involves development of artificial neurons and synapses. More studies have hitherto been focused on artificial synapses instead of neurons because the latter should demonstrate leaky integrate-and-fire (LIF) properties, which is a challenge to replicate artificially. In this work, we propose a domain wall (DW) based device made from perpendicularly magnetized $(Co/Ni)_n$ nanowire (NW) with magnetic anisotropy and saturation magnetization gradients. The DW is current-driven via spin-transfer-torque. Micromagnetic simulations demonstrated that the DWs in NWs with anisotropy field gradients can automatically return towards the initial position when electrical current is absent, indicative of the leakage process. The underlying physics of DW motion in such structure was studied in detail. To replicate the crystallinity of $(Co/Ni)_n$ structures, granular NWs were also defined. Depending on the grain structure of the NW, it was found that LIF properties were achieved under the conditions of steep anisotropy field gradients. Therefore, the proposed design has potential applications in neuron devices.

1. Introduction

Artificial Intelligence (AI) has demonstrated the capability to tackle global issues such as pandemic detection [1]–[3], healthcare service improvement [4]–[6] and disaster forecasting [7]–[9]. Nevertheless, the potential application of AI is limited by the power consumption issues arising from the von Neumann architecture that the current devices rely on [10]–[12]. For instance, the energy required to train a cutting-edge supercomputer in natural language is equivalent to six years of brain activity [13]. Consequently, the brain-inspired neuromorphic computing (NC) has garnered significant attention recently as it is expected to be more power-efficient and a more suitable programming platform for AI [14]–[18].

The neuromorphic architecture comprises a network of interconnected synapses and neurons, each mimicking their biological counterpart [19]. The synapse is the memory component of the device, regulating the importance, known as 'weight', of the signals transmitted from the pre-synaptic neuron to the post-synaptic neuron. On the other hand, the neuron constitutes the processing unit of the brain. More importantly, neurons should perform the leaky integration of signals from synapses, and once the integrated signal strength is above a threshold, the neuron will fire and reset to ground state thereafter. The integration of input signals in a neuron is called depolarization, while the leakage of signal strength is termed repolarization [20].

Replication of the repolarization process poses a great challenge in the fabrication of artificial neurons, it should happen automatically whenever an input is absent. Studies have proposed designs that can automatically repolarize [21]–[23]. For instance, the simulation study of a skyrmion-based neuron device showed that the skyrmion can regress in position in the absence of current due to edge repulsion from the wedged device [22]. However, skyrmion detection was inconsistent, compromising the device reliability. Moreover, Amogh *et al.* proposed designs for a

high-aspect ratio domain wall (DW) based artificial neuron that relies on shape anisotropy to induce the leakage function [23], albeit the DW velocity may not follow a predictable pattern.

DW based devices have shown to be promising in the emerging fields of computing [21], [22], [24]–[26]. For instance, a ring-shaped DW racetrack memory design was proposed that could overcome the data overflow issue encountered by the conventional tape-shape racetrack memory [25]. Additionally, a four-terminal DW device that could function as both a memory cell and in-memory logic unit was presented [24], where simulations found that it was more energy efficient than STT-MRAM as memory cells; and less energy consuming than CMOS-ASIC as logic units. Finally, Sengupta *et al.* proposed designs for NC, specifically, DW based artificial neurons and synapses that implemented magnetic tunnel junctions (MTJs) [26]. The free layer consists of two domains separated by a DW. The DW is driven either by spin-transfer torque (STT) or spin-orbit-torque (SOT), depending on the structure of the device [27]. Several experimental works have been carried out on synapses too [27]–[31].

In this study, we designed an artificial neuron that is a nanowire (NW) which exhibits both magnetic anisotropy (K_u) and saturation magnetization (M_s) gradients. We expect the DW to propagate when current is applied; and return towards the initial position when the current is switched off. We performed micromagnetic simulations to systematically study this idea, choosing parameters that could be experimentally realized for $(Co/Ni)_n$ films [32]–[40]. It was found that the combination of the anisotropy field (H_k) gradient and interfacial Dzyaloshinskii-Moriya interaction (*i*DMI) was not only able to result in DW returning when current is switched off, the latter is responsible for the stabilization of DW around the starting position once it returns.

2. Simulation details

Design of the proposed three terminal magnetic tunnel junction (3T-MTJ) device is shown in **Fig. 1**. The free layer NW is the simulated system, and the DW is propagated via STT from applied electrical current [41]. The initial position of the DW is set at 128 nm from the left end of the NW. Before the DW reaches the position of the MTJ, the antiparallel (AP) configuration results in high tunnel magnetoresistance (TMR), and the neuron does not fire. Neuronal firing occurs when the DW position surpasses that of the MTJ, so that the parallel (P) configuration is achieved and the TMR is low. We set this position to be around 384 nm from the left edge of the NW. At this stage, the neuron will fire and reset to ground state afterwards, *i.e.* DW returns to and stabilizes around the initial position. To achieve that, the region of interest (ROI), as indicated in **Fig. 1**(a) which has K_u and M_s gradients, plays an important role.

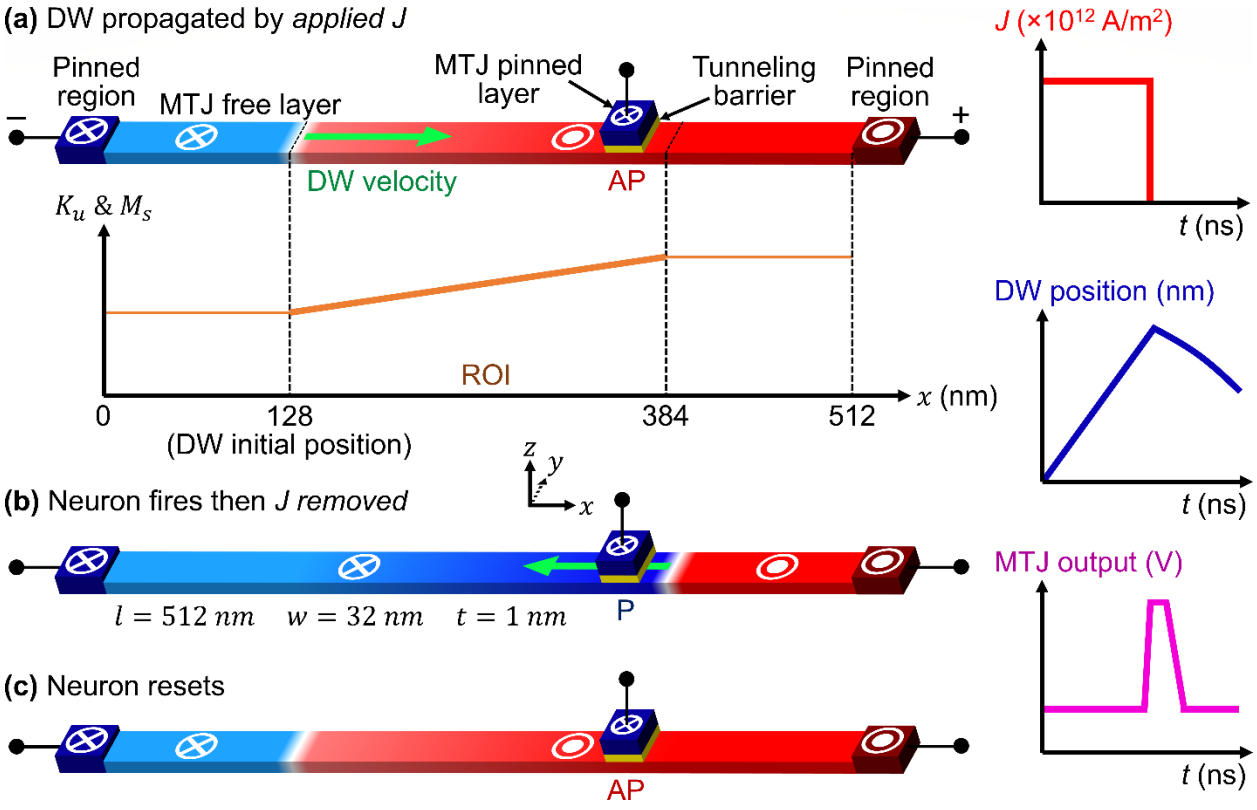

Fig. 1 The proposed three terminal (3T)-MTJ device. Magnetizations of the pinned layers are fixed while that of the MTJ free layer NW can be manipulated by applying electrical current. Conduction electrons are polarized by a pinned layer and push the DW by STT. Neuronal firing happens when the DW propagates past the MTJ device, *i.e.* when parallel configuration of the MTJ is achieved.

Simulations were performed on Mumax3 to show that the DWs can automatically return and stabilize around the initial position in the absence of applied electrical current [42]. The dimensions of the NWs are $512 \times 32 \times 1\ \text{nm}^3$, and the cell size is $2 \times 2 \times 1\ \text{nm}^3$, which is less than the exchange length ($l_{ex} \approx 6.09\ nm$) of the investigated magnetic system. The length of the ROI is 256 nm, and regions of constant K_u, M_s and anisotropy field (H_k) span 128 nm at both ends of the NW. The system is a two-domain perpendicular magnetic anisotropy (PMA) NW with uniaxial anisotropy along the z-axis. The left and right domains have $-z$ and $+z$ magnetizations, respectively.

The magnetic parameters used are: anisotropy constant $K_u = 0.4\ MJ/m^3$ [32]–[34], [37], saturation magnetization $M_s = 655\ kA/m$ [33]–[36], [39], exchange stiffness constant $A = 1 \times 10^{-11}\ J/m$ [32], [34], [37], [39], damping constant $\alpha = 0.02$ [33], [34], non-adiabaticity of spin-transfer-torque (STT) $\beta = 0.02$, and interfacial Dzyaloshinksii-Moriya strength $D = 0.25\ mJ/m^2$ [33], [34], [37]–[39]. These parameters can experimentally be achieved for $(Co/Ni)_n$ system [43]. Although single values of K_u and M_s are provided, they were varied to generate gradients as indicated in **Fig. 1**.

STT-driven DW motion is based on the extended Landau-Lifshitz-Gilbert (LLG) equation [44]:

$$\frac{d\vec{m}}{dt} = -\gamma_0 \vec{m} \times \vec{H} + \alpha \vec{m} \times \frac{d\vec{m}}{dt} - (\vec{u} \cdot \nabla)\vec{m} + \beta \vec{m} \times [(\vec{u} \cdot \nabla)\vec{m}] \quad (1)$$

Hence, $\gamma_0 = \frac{\mu_0 g e}{2m_e}$ is the gyromagnetic constant, $\vec{H}$ is the effective magnetic field acting on local reduced magnetic moment (with unit length) $\vec{m}$. In the present situation, $\vec{H}$ includes magnetostatic field, Heisenberg exchange field, Dzyaloshinksii-Moriya (DM) exchange field and anisotropy field [42]. $\vec{u}$ is a velocity vector along the direction of electron motion and is given by [44],

$$\vec{u} = J \frac{P g \mu_B}{2 e M_s} \hat{\imath} \quad (2)$$

Here, J is applied current density, current polarization is defined as $P = 0.5$ [40], g is Landé factor, μ_B is Bohr magneton, e is electronic charge and $\hat{\imath}$ is the unit vector along electron flow direction. The first term on the right side of Equation (1) is the precession torque while the second term is the damping torque. The third and fourth terms are the adiabatic STT and non-adiabatic STT respectively [44], and they are responsible for DW propagation under applied electrical current. When $\alpha = \beta$, DW undergoes steady motion with velocity given by [45], [46]:

$$\vec{v} = \vec{u} \quad (3)$$

Table 1 Compilation of parameters of the ROI of the NWs. Each set is represented by a codename in the leftmost column. H_k is calculated from $H_k = 2K_u/M_s$ [47].

Codename	K_u**(MJ/m³)**	M_s **(kA/m)**	H_k **(T)**
REF000	0.4	655	1.22
KM301	0.3 – 0.4	491.25 – 655	1.22
KM351	0.35 – 0.4	573.13 – 655	1.22
KM302	0.3 – 0.4	573.13 – 655	1.05 – 1.22
KM352	0.35 – 0.4	614.06 – 655	1.14 – 1.22

A summary of the simulated NW parameters is listed in **Table 1**. Each set is represented by a codename in the leftmost column. There are two types of M_s profiles; – (i) gradient at equal proportion $(\Delta M_s/M_s = \Delta K_u/K_u)$, and (ii) gradient at half proportion to K_u profile $(\Delta M_s/M_s = \Delta K_u/2K_u)$.

It may be useful to note that while this idea might not work at the industry scale, it is still possible to fabricate a NW with graded $H_k$in the laboratory using wedged structures [48], [49]. Experimental works on wedged structures will lead to further ideas which would eventually work at an industrial production level. Alternatively, one can also deposit a resist coating with a thickness gradient on the NW [50], then perform ion implantation whereby the dose of implanted ions can be tuned with the resist layer thickness to achieve a graded H_k profile.

3. Results and Discussions

To examine the DW motions of the NWs, we first look at the DW position (x) vs time (t) graphs. A current pulse is applied with specific pulse width (PW) to drive the DW to around 384 nm where the neuron will fire, as illustrated in **Fig. 1**(b). The pulse is then removed, and the subsequent DW motion is observed. **Fig. 2**(a) shows REF000, where the DW undergoes steady motion for all applied currents, consistent with Equation (3). After current application, the DW moves leftwards very slowly and does not return to initial position, even after 50 ns.

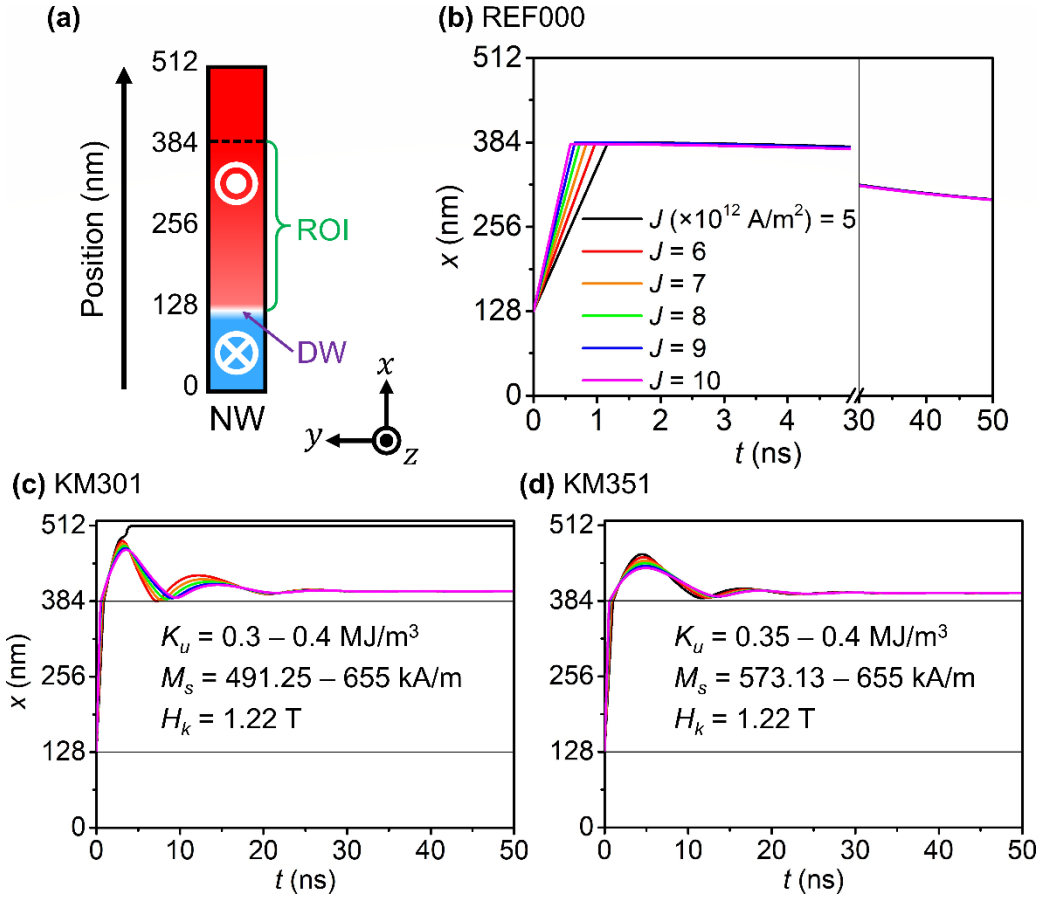

Fig. 2 (a) Schematic of the NW with ROI labelled. (b, c and d) DW position vs time graphs for the reference NW, KM301 and KM351. A single current pulse is applied to push the DWs from 128 *nm* to the 384 *nm* mark on the NW, *i.e.* across the ROI.

Fig. 2(b) and **Fig. 2**(c) show the results of KM301 and KM351 respectively. It is worth noting that these NWs, while exhibiting K_u and M_s gradients, have constant H_k. When current is switched off, the DWs do not return to the starting position. As such, we decided to introduce NWs with H_k gradients, and the results are shown in **Fig. 3**.

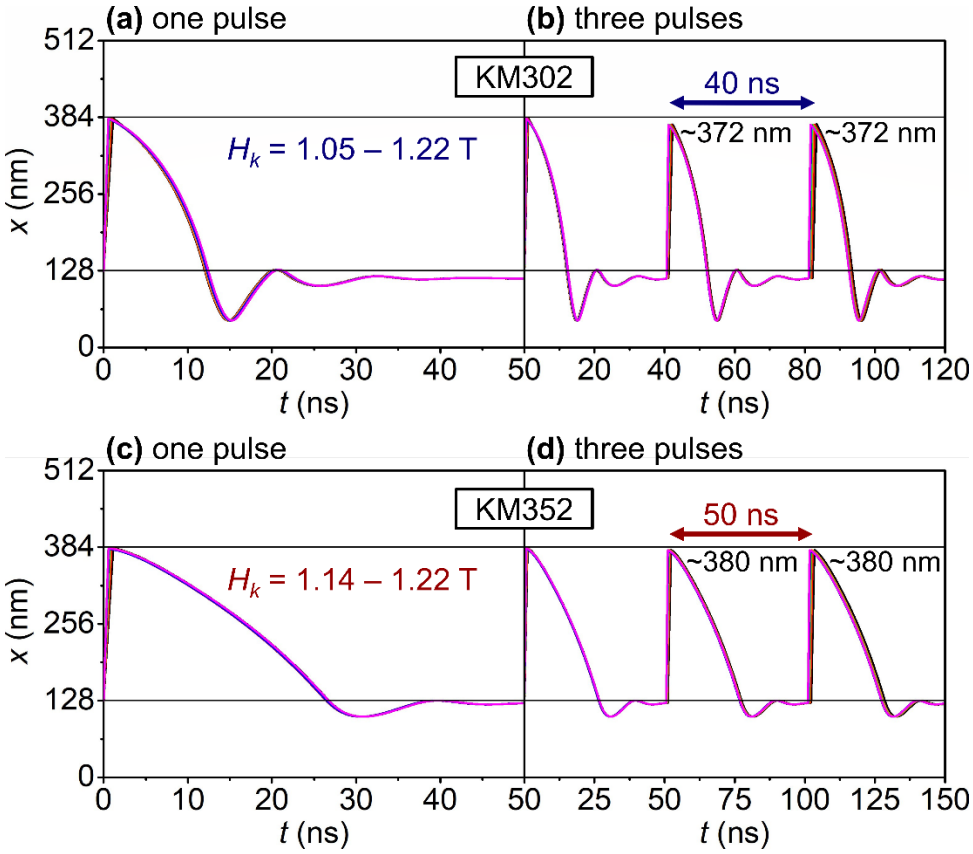

Fig. 3 NWs with DWs that can return to starting position after current is removed. (a and c) Cases whereby only a single current pulse is applied to push the DW. (b and d) Cases with three pulses sequentially applied in KM302 and KM352 respectively. The durations are the same between each pulse and are sufficient for the DWs to stabilize around the initial position before being propagated again.

Within these NWs, the DWs returned and stabilized around the initial position after reaching 384 nm (neuronal firing) and removing the current. When the NWs are resetting, the DWs are observed to undergo damped oscillatory motion around the initial position (DW position = 128 nm) before stabilizing. To find out the durations required by the DWs to stabilize, we refer to **Fig. 3**(b)

and **Fig. 3**(d). The intervals between the applied current pulses in **Fig. 3**(b) and **Fig. 3**(d) are the durations required by the DWs to return and stabilize around the initial position in each case. KM302 needs 40 ns to fully reset while KM352 requires 50 ns to do so.

Although the DW dynamics in both KM302 and KM352 are rather consistent with each successive identical pulse, there is a slight discrepancy in the DW dynamics in KM302 (**Fig. 3**(b)). The DW propagates to ~372 nm after the application of the second and third pulse even though they have the same magnitude and duration (PW) as the first pulse. However, this issue is relatively minor as the ROI spans 256 nm.

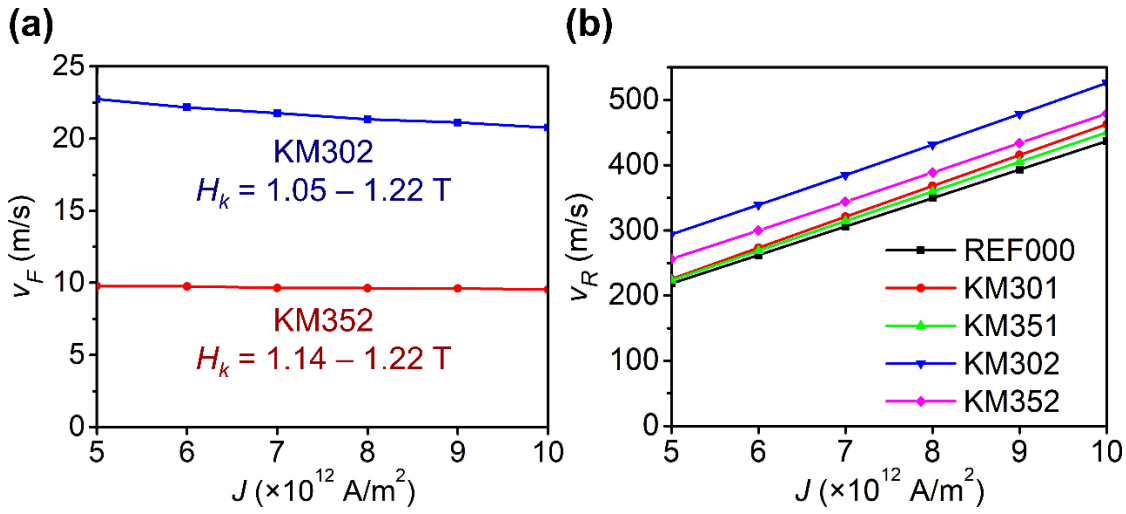

Fig. 4 (a) Curves of v_F against applied J for the two NWs that can be reset after firing. (b) Graph of v_R against J for all simulated NWs.

Now that KM302 and KM352 are determined as the NWs that can be reset after firing, we will assess the velocity of returning DW. **Fig. 4**(a) shows the velocity of DW 'falling' back (named as v_F) plotted against J. v_F can represent the speed of neuron repolarization [20]. KM302 has a higher v_F than KM352, which is comprehensible given that the former has a steeper H_k gradient.

What is more interesting is that v_F appears to vary with J. This is due to a combination of two factors; (i) different extent of DW precessions among different applied current pulses (J and PW),

coupled with (ii) the relationship between DW structure and its instantaneous velocity. The details of this will be discussed in the explanation of **Fig. 6**(a) and **Fig. 6**(b).

To develop a more complete view on the performance of the NWs, we will examine the DW propagation velocities under applied current, as shown in **Fig. 4**(b). This is related to the firing process of the neuron. The velocity of DW 'rising' towards the 384 nm point of the NW, named as v_R, is plotted against J. v_R is associated with the speed of neuron depolarization [20], and they range between $200 - 550$ m/s. One can observe that v_R appears to be increase linearly with J. That is certainly the case for REF000 according to Equations (2) and (3), where $v \propto J$. However, it may be important to note that the main objective of this work is to study the DW motion when current is switched off, which may put the DW dynamics in the presence of current in less emphasis.

Previously, we elucidated that DWs undergo precession within the ROI of the NWs, except REF000. Now, we will discuss the details behind this motion, using a detailed illustration of the DW dynamics of KM302 shown in **Fig. 5** [51]. At t_0, the DW starts off as a Néel wall with $+x$ magnetization at the center of the DW, which applies to all NWs. This is to align with the in-plane component of the interfacial-DM interaction (*i*DMI) exchange field ($\vec{B}_{iDMI}$) [42], which is in the $+x$ direction. To understand that, we refer to the expression of $\vec{B}_{iDMI}$:

$$\vec{B}_{iDMI} = \frac{2D}{M_s}\left(\frac{\partial m_z}{\partial x}, \frac{\partial m_z}{\partial y}, -\frac{\partial m_x}{\partial x} - \frac{\partial m_y}{\partial y}\right) \quad (4)$$

Here, D is the strength of *i*DMI field. The derivatives are computed as: $\frac{\partial \vec{m}}{\partial i} = \frac{\vec{m}_{i+1} - \vec{m}_{i-1}}{2\Delta_i}$, where $\vec{m}_{i+1}$ and $\vec{m}_{i-1}$ are magnetic moments of the two opposing neighbors adjacent to the central cell; Δ_i is the length of the cell along the i-axis. Referring to $\vec{B}_{iDMI}(x)$, knowing that the magnetizations of the left and right domains of the NW are $-z$ and $+z$ respectively, one may realize that $\frac{\partial m_z}{\partial x} > 0$.

Consequently, $\vec{B}_{iDMI}(x)$ will always be positive across the DW, and the DW will always start off as a $+x$ Néel wall as in **Fig. 5**(b) at t_0.

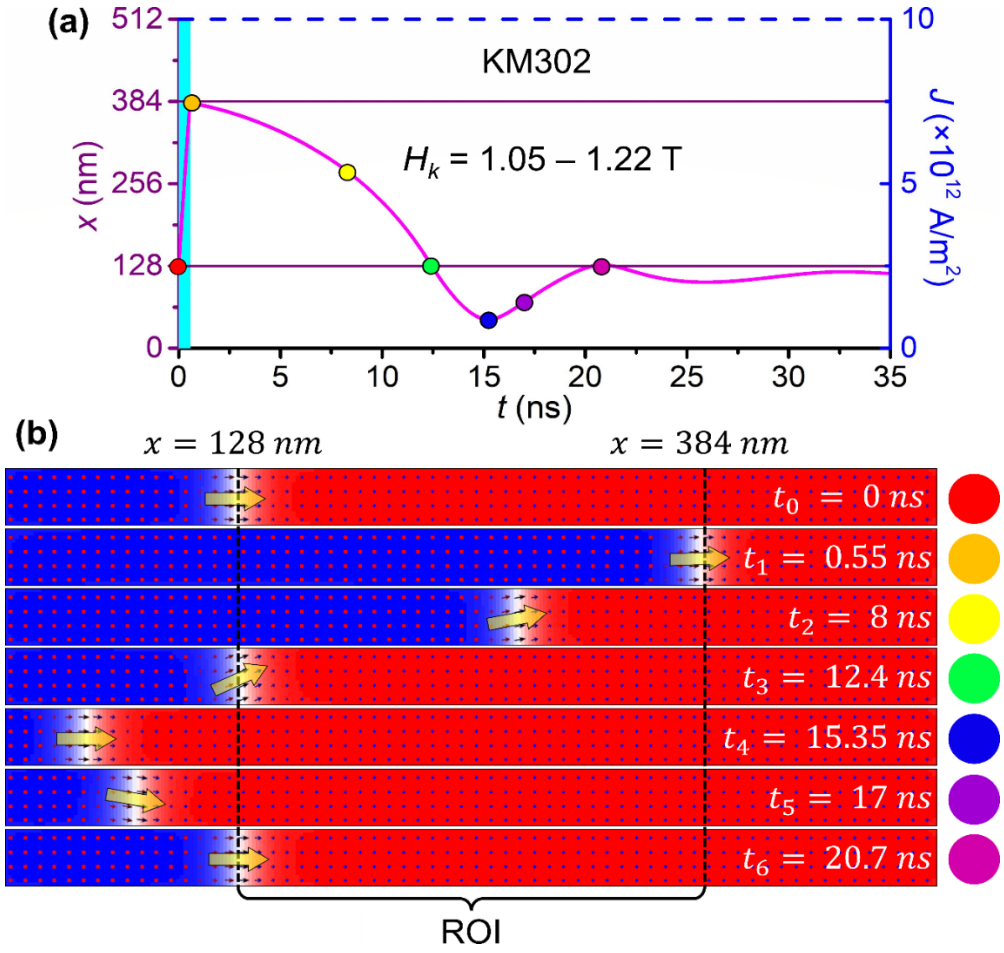

Fig. 5 Pictorial illustration of DW structures at various points in time. Seven spots were marked on the DW position vs time graph (a). Their associated NW images are shown in (b).

At the time t_1 of switching off the current, *i.e.* $0.55\ ns$, there is a minor change in DW structure relative to the initial point, indicating a slight precessional propagation ($\sim 2°$ in the anticlockwise (ACW) direction). One may refer to Supplementary Section S1 for a movie illustration. This is a result of the H_k gradient within the ROI, which is crucial in inducing the DW automatic returning motion. This H_k gradient affects the magnitude of the uniaxial magnetic anisotropy field ($\vec{B}_{anis}$), which is expressed as [42]:

$$\vec{B}_{anis} = \frac{2K_u}{\mu_0 M_s}(\hat{k}\cdot\vec{m})\hat{k} = \frac{H_k}{\mu_0}(\hat{z}\cdot\vec{m})\hat{z} \quad (5)$$

Here, $\hat{k} = +\hat{z}$, the unit vector along the anisotropy direction.

An H_k gradient gives a $|\vec{B}_{anis}|$ gradient, and hence, there will be a difference in $|\vec{B}_{anis}|$ across cells along the x direction. Specifically, $|\vec{B}_{anis}|$ is higher on the right side of the ROI than the left. The relevance of this is observed in **Fig. 6**(a). We examine the spins at the sides of the DW, which have out-of-plane components, to ensure $\vec{B}_{anis}$ is non-zero (Equation (5)). Due to the $|\vec{B}_{anis}|$ gradient, the left spins experience a weaker torque ($\vec{\tau} \propto (\vec{B}_{anis} \times \vec{m})$) while a stronger and opposite torque is exerted on the right. As a result of exchange interaction, the DW will be influenced to precess in the direction of the stronger torque on the right, and hence, undergo ACW precession. It is useful to note that the steeper the H_k gradient, the larger the difference between the two torques is in **Fig. 6**(a), the faster the precession.

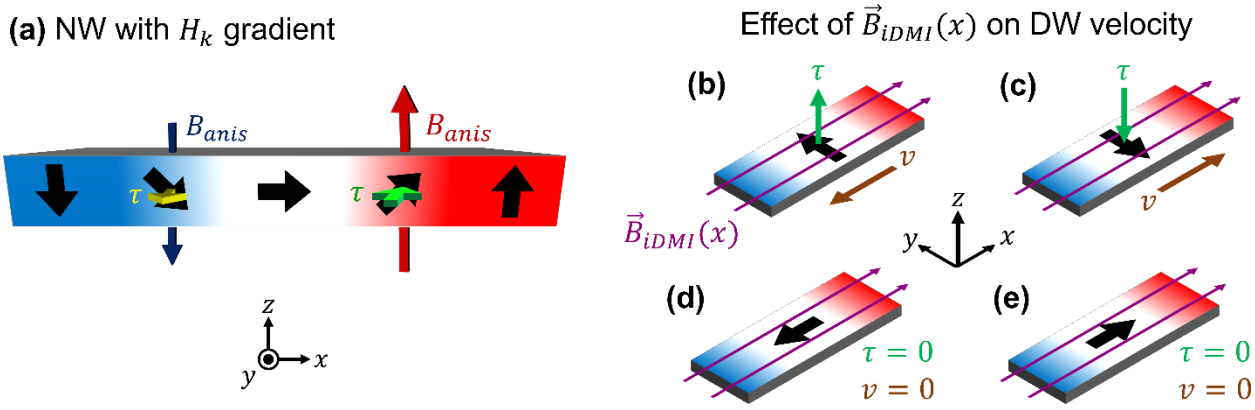

Fig. 6 (a) Illustration of the effect on DW by an H_k gradient. This effect only exists within the ROI of the NW. (b-e) Torque exerted by $\vec{B}_{iDMI}(x)$ on different DW structures. It is worth noting that this effect is present regardless of DW position.

As long as H_k gradient exists (within the ROI), DW ACW precession occurs even without current input (**Fig. 5**). Even after current is switched off, (from $t = 0.55 - 12.4\,ns$) the DW

precessed ~23° in the ACW direction. This is significantly more than the ~2° precession that happened from $t = 0 - 0.55\ ns$.

Another important observation from $t = 0.55 - 12.4\ ns$ is that the DW returns towards the initial position in the absence of current. This is due to the torque in +z axis exerted by $\vec{B}_{iDMI}(x)$ on the magnetizations within the DW ($\vec{\tau}_z \propto (\vec{B}_{iDMI}(x) \times \vec{m}(y))$) that pushes it leftwards, as illustrated in **Fig. 6** (b). It is important to note that while $\vec{B}_{iDMI}(x)$ is always positive across the DW, $\vec{m}(y)$ of DW is not fixed, due to the ACW precession explained previously that changes the DW structure. As such, we refer to **Fig. 6** (c-e) for the effect of $\vec{B}_{iDMI}(x)$ on other DW structures. It can be understood that a maximum torque is exerted on Bloch walls **Fig. 6**(b-c), because $\vec{B}_{iDMI}(x) \perp \vec{m}$ of the DW. Meanwhile, $\vec{B}_{iDMI}(x) \parallel \pm\vec{m}$ for Néel walls, and hence, no torque is exerted (**Fig. 6**(d-e)). Basically, the magnitude and direction of the torque exerted by $\vec{B}_{iDMI}(x)$ depends on $\vec{m}(y)$ of the DW. In the absence of current, Néel walls are instantaneously stationary, while Bloch walls exhibit local maximum speeds.

Returning to the discussion on **Fig. 5**, from $t = 12.4 - 20.7\ ns$, ACW precession stopped outside the ROI because there is no H_k gradient as in **Fig. 6**(a). Instead, only the effect from $\vec{B}_{iDMI}(x)$ remains outside ROI and the DW undergoes damped precession around $+x$ and eventually stabilizes along that direction. And every time the DW becomes a $+x$ Néel wall, it will be instantaneously stationary, as discussed earlier (**Fig. 6**(e)). It is until the magnetization precesses through $+x$ due to residual momentum that the DW moves, and in the opposite direction, as evident from $t = 12.4 - 17\ ns$. The reason is that the y-component of the DW magnetization has flipped, leading to an opposite torque exerted by $\vec{B}_{iDMI}(x)$, resulting in a velocity in the reverse

direction. This continues until the DW loses momentum and stabilizes as a $+x$ Néel wall, similar to a damped oscillatory motion.

To sum up, the phenomena of DW automatically returning depends on two properties, i.e. H_k gradient and *i*DMI. Initially, DW starts off as a $+x$ Néel wall, which is stabilized by *i*DMI. As current drives DW to travel within the ROI, the H_k gradient causes it to precess ACW, giving the DW a $+y$ magnetization component. Referring to **Fig. 6**(b), the torque from $\vec{B}_{iDMI}(x)$ will push the DW leftwards, resulting in the returning motion when current is switched off.

Now, we are equipped to understand the dependence of v_F on J evident in **Fig. 4**(a). First, we will focus on the period where current is applied, *i.e.* from $t = 0\ ns$ to $t = PW$. The higher the J, the lower the PW required to propagate the DW towards the 384 nm mark of the NW, the shorter the duration that the DW spends within the ROI (with H_k gradient), the lower the extent of DW ACW precession at $t = PW$ as seen in **Table 2**. As a result, the higher the J, the slower the 'falling' velocity when current is switched off (for $t > PW$). This explains why in **Fig. 4**(a), v_F decreases with increasing J for KM302.

Table 2 Compilation of angles precessed by DW in the ACW direction from $t = 0\ ns$ to $t = PW$.

KM302			**KM352**		
J $(\times 10^{12}\ A/m^2)$	PW (ns)	ACW precession angle (°)	J $(\times 10^{12}\ A/m^2)$	PW (ns)	ACW precession angle (°)
5	1.13	4.0°	5	1.14	1.5°
6	0.93	3.5°	6	0.94	1.4°
7	0.79	2.8°	7	0.81	1.3°
8	0.69	2.5°	8	0.705	1.2°
9	0.61	2.2°	9	0.625	1.1°
10	0.55	2.0°	10	0.565	1.0°

It is important to note that the same dependence of v_F on J is less observable for KM352. This is because KM352 has a gentler H_k gradient than KM302 ($\Delta H_k = 0.08\,T$ vs $\Delta H_k = 0.17\,T$), and that means the rate of ACW precession in the former is slower than the latter, hence the variation in precession extent is less significant in KM352 than in KM302, as shown in **Table 2**. Furthermore, due to the lower rate of ACW precession in KM352, the $+y$-component of the DW at $t = PW$ is lower relative to that in KM302, and thus, v_F is lower as well, which is evident in **Fig. 4**(a).

A compilation of DW motions is shown in **Table 3**. Since KM301 and KM351 did not display the leaky integrate-and-fire behavior [19], the physics behind the DW clockwise (CW) precession will be explained in Supplementary Section S3. In that section, the Heisenberg exchange field ($\vec{B}_{H\_exch}$) will be discussed.

Table 3 Compilation of the DW precession within the ROI for all data sets in **Table 1**. It may be noted that this precession happens within the ROI regardless of applied current.

NWs	H_k **(T)**	**Precession (within ROI)**
REF000	1.22	Unobservable
KM301, KM351	1.22 1.22	CW
KM302, KM352	1.05 – 1.22 1.14 – 1.22	ACW

We then determined the critical current densities (J_c) of KM302 and KM352; and found that J_c of KM302 is $2 \times 10^{12}\ A/m^2$ while $J_c \sim 10^{11}\ A/m^2$ for KM352. J_c is an approximate for KM352 because we limited the current pulse width to be $10\ ns$ maximum, and in that case, $J = 7 \times 10^{11}\ A/m^2$ took more than $10\ ns$ to push the DW towards the $384\ nm$ mark of the NW. On

a different note, it was found that LIF properties were demonstrated in both NWs regardless of the strength of J, as illustrated in **Fig. 7**.

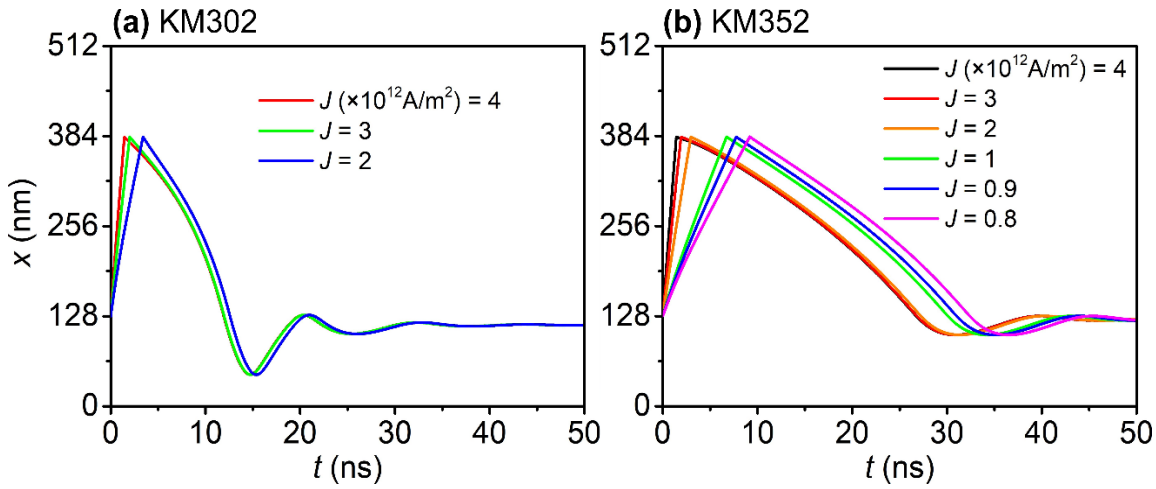

Fig. 7 DW position vs time graphs for (a) KM302 and (b) KM352. DWs are able to automatically reset its position, indicative of the leakage function and hence, LIF properties are displayed.

This finding further supports the validity of KM352 because not only is the DW motion consistent, the critical current density is also in the magnitude of $10^{11}\ A/m^2$, which is within typical experimental values [52]–[54]. Lastly, LIF properties are preserved as well.

Granted, the crystallinity of Co/Ni multilayers can be detrimental to the DW motion. Not only could it increase the J_c of the sample, it may also complicate the process of achieving LIF properties in an artificial neuron. Therefore, we have also introduced grains in the form of Voronoi cells in the system [42], with mean grain size of $20\ nm$, anisotropy direction to vary by 3°, exchange interaction among grains to scale from $90\% - 100\%$, and K_u and M_s values to fluctuate from $97.5\% - 100\%$ [55]–[58]. The definition of grains requires one to set a random seed, and different random seeds result in NWs of different grain shapes and sizes, as well as varying K_u and M_s profiles shown in **Fig. 8**(a), associated to the NWs with $K_u \approx 350 - 400\ kJ/m^3$, $M_s \approx 614 - 655\ kA/m$ and $H_k \approx 1.14 - 1.22\ T$.

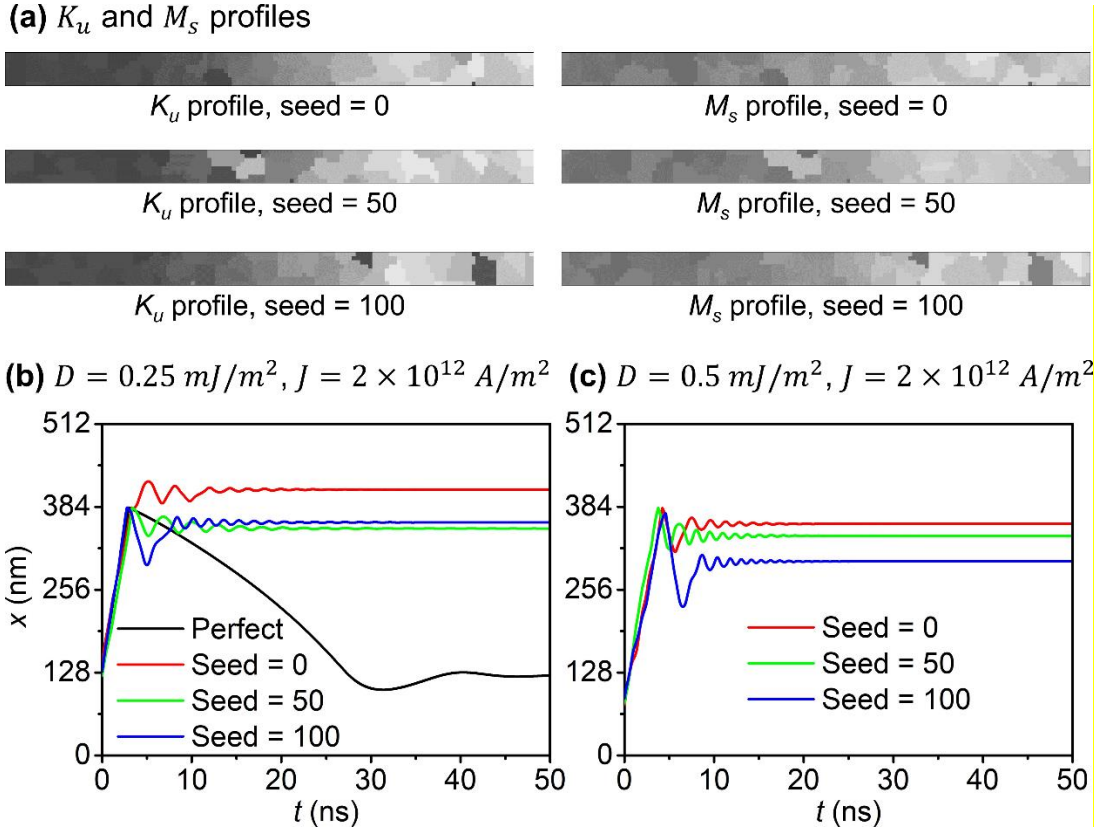

Fig. 8(a) $K_u \approx 350 - 400\ kJ/m^3$ and $M_s \approx 614 - 655\ kA/m$ profiles of NWs with different random seeds. The lighter shades represent higher values, vice versa. DW position vs time graphs for NWs with $H_k \approx 1.14 - 1.22\ T$, (b) $D = 0.25\ mJ/m^2$ and (c) $D = 0.5\ mJ/m^2$. The applied current density is $J = 2 \times 10^{12}\ A/m^2$.

Unsurprisingly, different grain structures lead to varying DW motions, which is evident in **Table 4** where the current pulse widths required to drive the DW to the threshold position are different. Moreover, once grains are defined, J_c is higher, *i.e.* $2 \times 10^{12}\ A/m^2$, while that of the perfect NW is $\sim 10^{11}\ A/m^2$. At $J = 2 \times 10^{12}\ A/m^2$, the pulse widths vary among granular NWs of different random seeds due to their different grain structures (**Fig. 8**(a)). Movie illustrations of DW motions in the granular NWs can be found in Supplementary Section S5.

Table 4 Compilation of pulse widths required by a specific applied current density (J) to push the DW to the threshold position in the NWs of $H_k \approx 1.14 - 1.22\ T$. The pulse widths are limited to a maximum of $10\ ns$, above which, will be denoted as '$> 10\ ns$'. 'N.A.' suggests that the DW is

unable to be propagated to the threshold position regardless of duration of current application, implying that $J < J_c$.

J (A/m^2)	Perfect	Granular (seed = 0)	Granular (seed = 50)	Granular (seed = 100)
4×10^{12}	1.43 ns	1.415 ns	1.525 ns	1.415 ns
3×10^{12}	1.925 ns	1.95 ns	2.08 ns	1.87 ns
2×10^{12}	2.96 ns	3.295 ns	3.36 ns	2.765 ns
1×10^{12}	6.73 ns	N.A.	N.A.	N.A.
9×10^{11}	7.75 ns	N.A.	N.A.	N.A.
8×10^{11}	9.17 ns	N.A.	N.A.	N.A.
7×10^{11}	> 10 ns	N.A.	N.A.	N.A.

Another drawback of a granular structure is that the DW is unable to return for this particular H_k gradient, as seen in **Fig. 8**(b). We tried to increase the *i*DMI strength because $\vec{B}_{iDMI}$ is crucial in the DW returning and stabilizing, from $D = 0.25\ mJ/m^2$ to $D = 0.5\ mJ/m^2$ (**Fig. 8**(c)), but to no avail. However, for steeper H_k gradients, we found that stronger *i*DMI strength does yield more NWs that exhibit LIF properties. That can first be observed for NWs with $H_k \approx 1.05 - 1.22\ T$ ($K_u = 300 - 400\ kJ/m^3$ and $M_s \approx 573 - 655\ kA/m$), in **Fig. 9**.

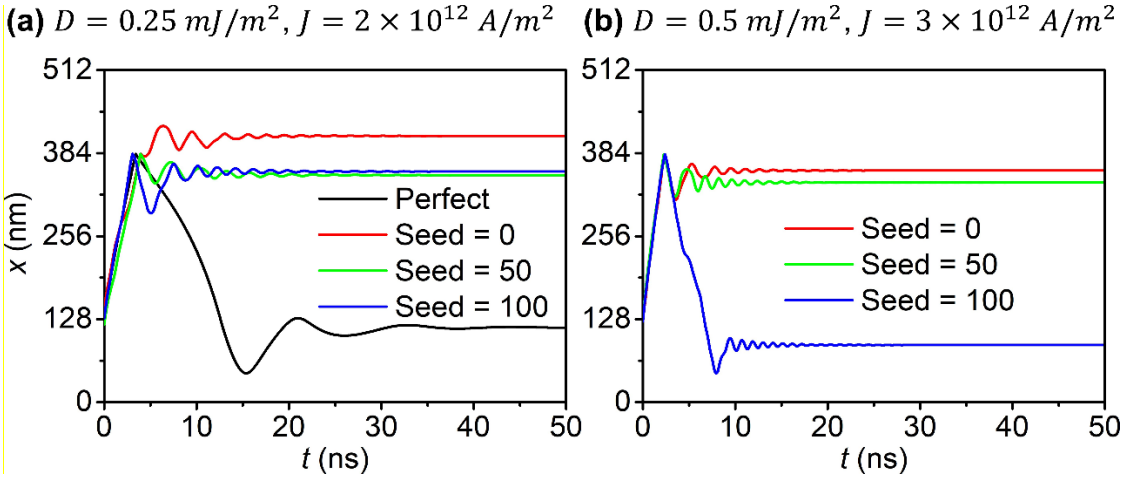

Fig. 9 DW position vs time graphs for NWs with $H_k \approx 1.14 - 1.22\ T$ and J is equivalent to the J_c of the perfect and granular cases within each graph, (a) $J_c = 2 \times 10^{12}\ A/m^2$ and (b) $J_c = 3 \times 10^{12}\ A/m^2$.

Referring to **Fig. 9**(b), by increasing *i*DMI strength to $D = 0.5\ mJ/m^2$, it is possible to achieve the LIF properties in the NW. Specifically, one granular NW with random seed 100 exhibited the LIF properties, albeit the DW stabilized at around 88 nm instead of the initial position at 128 nm. On the contrary, DWs in other conditions were unable to return, as tabulated in **Table 5**.

Table 5 Compilation of pulse widths required to push the DW in NWs of $H_k \approx 1.05 - 1.22\ T$, with different random seeds and *i*DMI strength. The top half comprises NWs of $D = 0.25\ mJ/m^2$ while those in the bottom half have $D = 0.5\ mJ/m^2$. The highlighted (shaded) cell with bold text represents the condition where LIF properties are achieved.

$\boldsymbol{H_k \approx 1.05 - 1.22\ T, D = 0.25\ mJ/m^2}$			
$\boldsymbol{J\ (A/m^2)}$	**Seed = 0**	**Seed = 50**	**Seed = 100**
4×10^{12}	1.42 ns	1.55 ns	1.415 ns
3×10^{12}	2.02 ns	2.185 ns	1.92 ns
2×10^{12}	3.98 ns	3.92 ns	3.07 ns
1×10^{12}	N.A.	N.A.	N.A.
$\boldsymbol{H_k \approx 1.05 - 1.22\ T, D = 0.5\ mJ/m^2}$			
$\boldsymbol{J\ (A/m^2)}$	**Seed = 0**	**Seed = 50**	**Seed = 100**
4×10^{12}	1.58 ns	1.56 ns	1.6 ns
3×10^{12}	2.3 ns	2.27 ns	**2.39 ns**
2×10^{12}	N.A.	N.A.	N.A.
1×10^{12}	N.A.	N.A.	N.A.

A disadvantage with increasing *i*DMI strength is that it will hinder DW motion, resulting in a higher J_c, and in this case (**Fig. 9**(b)), $J_c = 3 \times 10^{12}\ A/m^2$. Furthermore, only one granular NW is appropriate as an artificial neuron. We want to increase the number of conditions that give NWs with LIF properties. To that end, we increased the steepness of K_u and M_s gradients to $K_u =$

$280 - 400\ kJ/m^3$ and $M_s \approx 557 - 655\ kA/m$, so that $H_k \approx 1.01 - 1.22\ T$. The DW position vs time graphs are depicted in **Fig. 10**.

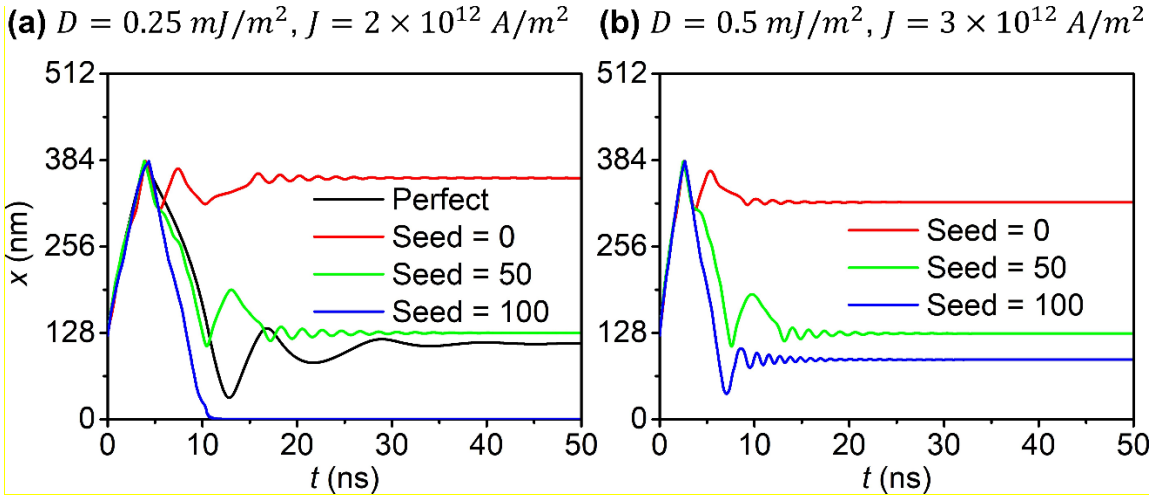

Fig. 10 DW position vs time graphs for NWs with $H_k \approx 1.01 - 1.22\ T$ and $J = J_c$.

Here, we notice that by increasing H_k gradient steepness, more conditions display the LIF properties. In **Fig. 10**(a), directly comparing the perfect NW (black curve) and the granular NW with random seed 50 (green curve), one may observe that the latter curve is more jagged, which is understandable given the granular condition. For a clearer illustration of this comparison, movies can be found in Supplementary Section S5. A compilation of the data pertaining to NWs with $H_k \approx 1.01 - 1.22\ T$ is found in **Table 6**.

Table 6 Compilation of pulse widths required to push the DW in NWs of $H_k \approx 1.01 - 1.22\ T$, with different random seeds and *i*DMI strength. The highlighted (shaded) cell with bold text represents the condition where LIF properties are achieved.

$\boldsymbol{H_k \approx 1.01 - 1.22\ T, D = 0.25\ mJ/m^2}$			
$\boldsymbol{J\ (A/m^2)}$	**Seed = 0**	**Seed = 50**	**Seed = 100**
4×10^{12}	$1.505\ ns$	$1.495\ ns$	$\mathbf{1.515\ ns}$
3×10^{12}	$2.125\ ns$	$2.105\ ns$	$\mathbf{2.17\ ns}$
2×10^{12}	$4\ ns$	$\mathbf{3.87\ ns}$	$4.35\ ns$
1×10^{12}	N.A.	N.A.	N.A.

$H_k \approx 1.01 - 1.22\ T, D = 0.5\ mJ/m^2$			
$J\ (A/m^2)$	**Seed = 0**	**Seed = 50**	**Seed = 100**
4×10^{12}	1.64 ns	1.63 ns	**1.67 ns**
3×10^{12}	2.53 ns	**2.49 ns**	**2.66 ns**
2×10^{12}	N.A.	N.A.	N.A.
1×10^{12}	N.A.	N.A.	N.A.

In light of the finding that steeper H_k gradients may yield more appropriate results, we decided to set an even steeper gradient of $K_u = 250 - 400\ kJ/m^3$ and $M_s \approx 532 - 655\ kA/m$, so that $H_k \approx 0.94 - 1.22\ T$. We realized that this gradient might be too steep and does not yield as many NWs that exhibit LIF properties, as illustrated in **Fig. 11**.

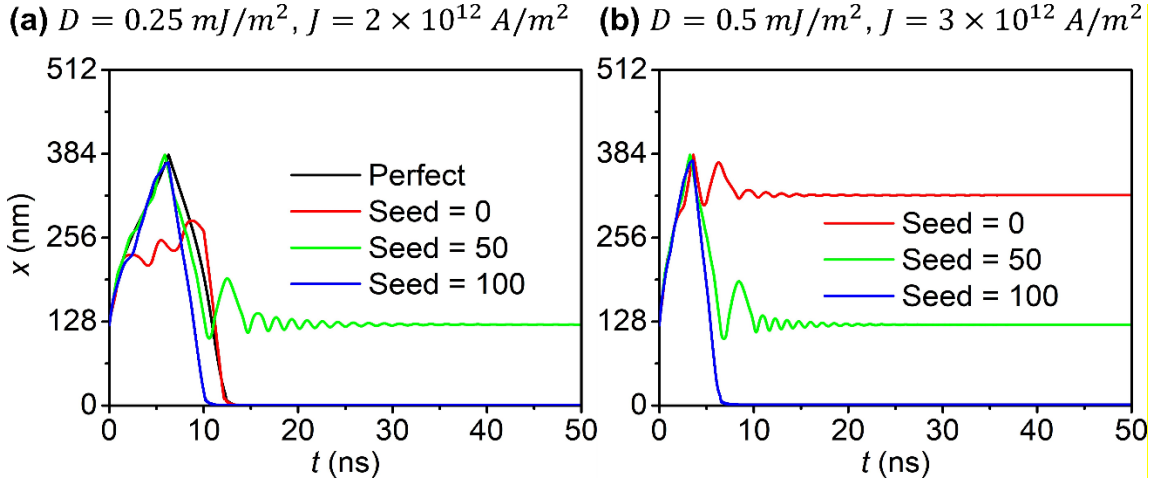

Fig. 11 DW position vs time graphs for NWs with $H_k \approx 0.94 - 1.22\ T$ and $J = J_c$.

At this gradient, even for $D = 0.25\ mJ/m^2$, J_c may be higher than $2 \times 10^{12}\ A/m^2$, depending on the grain structure of the NW, as evident in the NW with $D = 0.25\ mJ/m^2$ and random seed = 0 where the current is unable to propagate the DW to the threshold position within $10\ ns$. Furthermore, there are actually less conditions where LIF properties were achieved compared to those of $H_k \approx 1.01 - 1.22\ T$, as shown in **Table 7**. In fact, DWs were more likely to return but

unable to stabilize around the initial position. Even the DW in the perfect NW (**Fig. 11**(a) black curve) could not stabilize around initial position, indicating that this gradient may be too steep. Movies of DW motions in the NWs associated to the conditions in **Fig. 11**(a) are provided in Supplementary Section S5.

Table 7 Compilation of pulse widths required to push the DW in NWs of $H_k \approx 0.94 - 1.22\ T$, with different random seeds and *i*DMI strength. The highlighted (shaded) cells with bold text represent the conditions where LIF properties are achieved.

$\boldsymbol{H_k \approx 0.94 - 1.22\ T, D = 0.25\ mJ/m^2}$			
$\boldsymbol{J\ (A/m^2)}$	**Seed = 0**	**Seed = 50**	**Seed = 100**
4×10^{12}	1.56 ns	1.57 ns	1.58 ns
3×10^{12}	2.32 ns	**2.315 ns**	2.38 ns
2×10^{12}	N.A.	**5.88 ns**	6.25 ns
1×10^{12}	N.A.	N.A.	N.A.
$\boldsymbol{H_k \approx 0.94 - 1.22\ T, D = 0.5\ mJ/m^2}$			
$\boldsymbol{J\ (A/m^2)}$	**Seed = 0**	**Seed = 50**	**Seed = 100**
4×10^{12}	1.805 ns	**1.805 ns**	**1.85 ns**
3×10^{12}	3.59 ns	**3.25 ns**	3.54 ns
2×10^{12}	N.A.	N.A.	N.A.
1×10^{12}	N.A.	N.A.	N.A.

Therefore, we determined the optimum H_k gradient to be $H_k \approx 1.01 - 1.22\ T$ because it yields the most conditions where the NWs exhibit LIF properties. The steeper conditions also allow for more practical realization of the device. On a different note, increasing *i*DMI strength may improve the likelihood of getting designs suitable for artificial neurons, but at the expense of writability. Lastly, DW motions are strongly dependent on the grain structure of the NW.

4. Conclusion

We have proposed a domain wall (DW) device, that is a nanowire (NW) with graded magnetic anisotropy (K_u) and saturation magnetization (M_s), for its effectiveness in the leaky function of neurons. It has been demonstrated that NWs with anisotropy field (H_k) gradients display the leaky integrate-and-fire behavior. Specifically, the DW could automatically return towards the starting position in the absence of electrical current, and eventually stabilize around it. The underlying physics was studied, elucidating the origins of DW velocities and precession. Moreover, we defined grains within the NW to replicate the crystallinity of Co/Ni multilayer structures and found that steeper H_k gradients yielded more conditions of achieving NWs exhibiting the leaky-integrate and fire properties. Lastly, it may be possible to implement this design in compensated ferrimagnets and antiferromagnets because the former has been experimentally demonstrated [59]–[62] and the latter theoretically studied [63]–[65] to exhibit larger DW velocities.

5. Conflict of interest

The authors declare no conflict of interest.

6. Acknowledgements

The authors acknowledge National Supercomputing Centre Singapore (NSCC) for providing computing facilities and the funding from National Research Foundation (NRF) Singapore for the grants NRF-CRP21-2018-003 and NRF2015-IIP003-001. Also, the authors would like to thank Mr Sabpreet Bhatti for his advice on the simulations. Finally, WM and DK would like to thank NTU research scholarship for the financial support.

References

[1] L. Li *et al.*, "Artificial Intelligence Distinguishes COVID-19 from Community Acquired Pneumonia on Chest CT," *Radiology*, p. 200905, Mar. 2020, doi: 10.1148/radiol.2020200905.

[2] Z. Hu, Q. Ge, S. Li, L. Jin, and M. Xiong, "Artificial Intelligence Forecasting of Covid-19 in China," Feb. 2020, Accessed: Jun. 25, 2020. [Online]. Available: http://arxiv.org/abs/2002.07112.

[3] K. L. Tsui, Z. S. Y. Wong, D. Goldsman, and M. Edesess, "Tracking infectious disease spread for global pandemic containment," *IEEE Intell. Syst.*, vol. 28, no. 6, pp. 60–64, Nov. 2013, doi: 10.1109/MIS.2013.149.

[4] S. H. Park and K. Han, "Methodologic Guide for Evaluating Clinical Performance and Effect of Artificial Intelligence Technology for Medical Diagnosis and Prediction," *Radiology*, vol. 286, no. 3, pp. 800–809, Mar. 2018, doi: 10.1148/radiol.2017171920.

[5] Y. Zang, F. Zhang, C. A. Di, and D. Zhu, "Advances of flexible pressure sensors toward artificial intelligence and health care applications," *Materials Horizons*, vol. 2, no. 2. Royal Society of Chemistry, pp. 140–156, Feb. 23, 2015, doi: 10.1039/c4mh00147h.

[6] F. Amato, A. López, E. M. Peña-Méndez, P. Vaňhara, A. Hampl, and J. Havel, "Artificial neural networks in medical diagnosis," *Journal of Applied Biomedicine*, vol. 11, no. 2. University of South Bohemia, pp. 47–58, Jan. 01, 2013, doi: 10.2478/v10136-012-0031-x.

[7] X. Zhu, G. Zhang, and B. Sun, "A comprehensive literature review of the demand forecasting methods of emergency resources from the perspective of artificial intelligence," *Nat. Hazards*, vol. 97, no. 1, pp. 65–82, May 2019, doi: 10.1007/s11069-019-03626-z.

[8] A. Jalalkamali, M. Moradi, and N. Moradi, "Application of several artificial intelligence models and ARIMAX model for forecasting drought using the Standardized Precipitation Index," *Int. J. Environ. Sci. Technol.*, vol. 12, no. 4, pp. 1201–1210, Nov. 2015, doi: 10.1007/s13762-014-0717-6.

[9] T. R. V. Anandharajan, G. A. Hariharan, K. K. Vignajeth, R. Jijendiran, and Kushmita, "Weather Monitoring Using Artificial Intelligence," in *Proceedings - International Conference on Computational Intelligence and Networks*, Aug. 2016, vol. 2016-January, pp. 106–111, doi: 10.1109/CINE.2016.26.

[10] R. A. Nawrocki, R. M. Voyles, and S. E. Shaheen, "A Mini Review of Neuromorphic Architectures and Implementations," *IEEE Trans. Electron Devices*, vol. 63, no. 10, pp. 3819–3829, 2016, doi: 10.1109/TED.2016.2598413.

[11] B. Rajendran, A. Sebastian, M. Schmuker, N. Srinivasa, and E. Eleftheriou, "Low-Power Neuromorphic Hardware for Signal Processing Applications: A review of architectural and system-level design approaches," *IEEE Signal Process. Mag.*, vol. 36, no. 6, pp. 97–110, 2019, doi: 10.1109/MSP.2019.2933719.

[12] J. Fairfield, "Smarter machines," *Phys. World*, vol. 30, no. 3, pp. 33–36, 2017, doi: 10.1088/2058-7058/30/3/36.

[13] D. Marković, A. Mizrahi, D. Querlioz, and J. Grollier, "Physics for neuromorphic computing," *Nat. Rev. Phys.*, pp. 1–12, Jul. 2020, doi: 10.1038/s42254-020-0208-2.

[14] H. Farkhani, M. Tohidi, S. Farkhani, J. K. Madsen, and F. Moradi, "A Low-Power High-Speed Spintronics-Based Neuromorphic Computing System Using Real-Time Tracking Method," *IEEE J. Emerg. Sel. Top. Circuits Syst.*, vol. 8, no. 3, pp. 627–638, Sep. 2018, doi: 10.1109/JETCAS.2018.2813389.

[15] J. Torrejon *et al.*, "Neuromorphic computing with nanoscale spintronic oscillators," *Nature*, vol. 547, no. 7664, pp. 428–431, Jul. 2017, doi: 10.1038/nature23011.

[16] S. Choi *et al.*, "SiGe epitaxial memory for neuromorphic computing with reproducible high performance based on engineered dislocations," *Nat. Mater.*, vol. 17, no. 4, pp. 335–340, Apr. 2018, doi: 10.1038/s41563-017-0001-5.

[17] I. Boybat *et al.*, "Neuromorphic computing with multi-memristive synapses," *Nat. Commun.*, vol. 9, no. 1, pp. 1–12, Dec. 2018, doi: 10.1038/s41467-018-04933-y.

[18] Z. Wang *et al.*, "Engineering incremental resistive switching in TaO: X based memristors for brain-inspired computing," *Nanoscale*, vol. 8, no. 29, pp. 14015–14022, Aug. 2016, doi: 10.1039/c6nr00476h.

[19] J. Grollier, D. Querlioz, K. Y. Camsari, K. Everschor-Sitte, S. Fukami, and M. D. Stiles, "Neuromorphic spintronics," *Nat. Electron.*, 2020, doi: 10.1038/s41928-019-0360-9.

[20] I. M. Raman and B. P. Bean, "Resurgent sodium current and action potential formation in dissociated cerebellar Purkinje neurons," *J. Neurosci.*, vol. 17, no. 12, pp. 4517–4526, 1997, doi: 10.1523/jneurosci.17-12-04517.1997.

[21] W. H. Brigner *et al.*, "Graded-Anisotropy-Induced Magnetic Domain Wall Drift for an Artificial Spintronic Leaky Integrate-and-Fire Neuron," *IEEE J. Explor. Solid-State Comput. Devices Circuits*, vol. 5, no. 1, pp. 19–24, 2019, doi: 10.1109/JXCDC.2019.2904191.

[22] X. Chen *et al.*, "A compact skyrmionic leaky-integrate-fire spiking neuron device," *Nanoscale*, vol. 10, no. 13, pp. 6139–6146, 2018, doi: 10.1039/c7nr09722k.

[23] A. Agrawal and K. Roy, "Mimicking leaky-integrate-fire spiking neuron using automotion of domain walls for energy-efficient brain-inspired computing," *IEEE Trans. Magn.*, vol. 55, no. 1, 2019, doi: 10.1109/TMAG.2018.2882164.

[24] S. Angizi, Z. He, N. Bagherzadeh, and D. Fan, "Design and evaluation of a spintronic in-memory processing platform for nonvolatile data encryption," *IEEE Trans. Comput. Des. Integr. Circuits Syst.*, vol. 37, no. 9, pp. 1788–1801, 2018, doi: 10.1109/TCAD.2017.2774291.

[25] G. Wang *et al.*, "Ultra-Dense Ring-Shaped Racetrack Memory Cache Design," *IEEE Trans. Circuits Syst. I Regul. Pap.*, vol. 66, no. 1, pp. 215–225, 2019, doi: 10.1109/TCSI.2018.2866932.

[26] A. Sengupta, P. Panda, P. Wijesinghe, Y. Kim, and K. Roy, "Magnetic tunnel junction mimics stochastic cortical spiking neurons," *Sci. Rep.*, vol. 6, no. July, pp. 1–9, 2016, doi:

10.1038/srep30039.

[27] T. Jin, W. Gan, F. Tan, N. R. Sernicola, W. S. Lew, and S. N. Piramanayagam, "Synaptic element for neuromorphic computing using a magnetic domain wall device with synthetic pinning sites," *J. Phys. D. Appl. Phys.*, vol. 52, no. 44, pp. 0–5, 2019, doi: 10.1088/1361-6463/ab35b7.

[28] N. Sato *et al.*, "Domain Wall Based Spin-Hall Nano-Oscillators," *Phys. Rev. Lett.*, vol. 123, no. 5, p. 57204, 2019, doi: 10.1103/PhysRevLett.123.057204.

[29] J. Cai, B. Fang, C. Wang, and Z. Zeng, "Multilevel storage device based on domain-wall motion in a magnetic tunnel junction," *Appl. Phys. Lett.*, vol. 111, no. 18, pp. 1–5, 2017, doi: 10.1063/1.5002632.

[30] W. A. Borders *et al.*, "Analogue spin-orbit torque device for artificial-neural-network-based associative memory operation," *Appl. Phys. Express*, vol. 10, no. 1, pp. 1–5, 2017, doi: 10.7567/APEX.10.013007.

[31] Y. Cao, A. W. Rushforth, Y. Sheng, H. Zheng, and K. Wang, "Tuning a Binary Ferromagnet into a Multistate Synapse with Spin–Orbit-Torque-Induced Plasticity," *Adv. Funct. Mater.*, vol. 29, no. 25, pp. 1–8, 2019, doi: 10.1002/adfm.201808104.

[32] V. D. Tsiantos, T. Schrefl, D. Suess, W. Scholz, J. Fidler, and J. M. Gonzales, "Micromagnetic simulations of magnetization reversal in Co/Ni multilayers," *Phys. B Condens. Matter*, vol. 306, no. 1–4, pp. 38–43, 2001, doi: 10.1016/S0921-4526(01)00963-2.

[33] T. Koyama *et al.*, "Wire width dependence of threshold current density for domain wall motion in Co/Ni nanowires," *IEEE Trans. Magn.*, vol. 47, no. 10, pp. 3089–3091, 2011, doi: 10.1109/TMAG.2011.2157308.

[34] K. Yamada *et al.*, "Influence of instabilities on high-field magnetic domain wall velocity in (Co/Ni) nanostrips," *Appl. Phys. Express*, vol. 4, no. 11, pp. 19–22, 2011, doi: 10.1143/APEX.4.113001.

[35] T. Jin *et al.*, "Tilted magnetisation for domain wall pinning in racetrack memory," *J. Magn. Magn. Mater.*, vol. 489, no. April, p. 165410, 2019, doi: 10.1016/j.jmmm.2019.165410.

[36] X. Su *et al.*, "Evolution of magnetic properties and domain structures in Co/Ni multilayers," *Jpn. J. Appl. Phys.*, vol. 55, no. 11, pp. 0–4, 2016, doi: 10.7567/JJAP.55.110306.

[37] S. Hozumi, K. Yamada, and Y. Nakatani, "Examination of Stability of Skyrmions Structure in Co/Ni Multilayer Films," vol. 556, no. 1962, pp. 1–1, 2018, doi: 10.1109/icaums.2016.8479667.

[38] D. K. Lau and B. S. Nanoengineering, "Experimental Evaluation of the Interfacial Dzyaloshinskii-Moriya Interaction in Co/Ni Magnetic Multilayers," 2018.

[39] A. Al Subhi and R. Sbiaa, "Journal of Magnetism and Magnetic Materials Control of magnetization reversal and domain structure in (Co / Ni) multilayers," *J. Magn. Magn. Mater.*, vol. 489, no. June, p. 165460, 2019, doi: 10.1016/j.jmmm.2019.165460.

[40] H. Tanigawa, T. Suzuki, S. Fukami, K. Suemitsu, N. Ohshima, and E. Kariyada, "Thickness dependence of current-induced domain wall motion in a Co/Ni multi-layer with out-of-plane anisotropy," *Appl. Phys. Lett.*, vol. 102, no. 15, 2013, doi: 10.1063/1.4802266.

[41] J. Grollier *et al.*, "Magnetic domain wall motion by spin transfer," *Comptes Rendus Phys.*, vol. 12, no. 3, pp. 309–317, 2011, doi: 10.1016/j.crhy.2011.03.007.

[42] A. Vansteenkiste, J. Leliaert, M. Dvornik, M. Helsen, F. Garcia-Sanchez, and B. Van Waeyenberge, "The design and verification of MuMax3," *AIP Adv.*, vol. 4, no. 10, pp. 1–22, 2014, doi: 10.1063/1.4899186.

[43] D. Kumar, P. Sengupta, R. Sbiaa, and S. N. Piramanayagam, "Spin transfer torque induced domain wall oscillations in ferromagnetic nanowire with a nanoscale Dzyaloshinskii–Moriya interaction region," *J. Magn. Magn. Mater.*, vol. 507, no. March, p. 166807, 2020, doi: 10.1016/j.jmmm.2020.166807.

[44] A. Thiaville, Y. Nakatani, J. Miltat, and Y. Suzuki, "Micromagnetic understanding of current-driven domain wall motion in patterned nanowires," *Europhys. Lett.*, vol. 69, no. 6, pp. 990–996, 2005, doi: 10.1209/epl/i2004-10452-6.

[45] J. Sampaio, J. Grollier, and P. J. Metaxas, "Domain Wall Motion in Nanostructures," *Handb. Surf. Sci.*, vol. 5, pp. 335–370, 2015, doi: 10.1016/B978-0-444-62634-9.00008-4.

[46] A. Mougin, M. Cormier, J. P. Adam, P. J. Metaxas, and J. Ferré, "Domain wall mobility, stability and Walker breakdown in magnetic nanowires," *Epl*, vol. 78, no. 5, pp. 0–6, 2007, doi: 10.1209/0295-5075/78/57007.

[47] T. Jin *et al.*, "Nanoscale Compositional Modification in Co/Pd Multilayers for Controllable Domain Wall Pinning in Racetrack Memory," *Phys. Status Solidi - Rapid Res. Lett.*, vol. 12, no. 10, pp. 1–7, 2018, doi: 10.1002/pssr.201800197.

[48] C. F. Pai, M. Mann, A. J. Tan, and G. S. D. Beach, "Determination of spin torque efficiencies in heterostructures with perpendicular magnetic anisotropy," *Phys. Rev. B*, vol. 93, no. 14, pp. 1–7, 2016, doi: 10.1103/PhysRevB.93.144409.

[49] A. Maziewski *et al.*, "Magnetization states and magnetization processes in nanostructures: From a single layer to multilayers," *Phys. Status Solidi Appl. Mater. Sci.*, vol. 211, no. 5, pp. 1005–1018, 2014, doi: 10.1002/pssa.201300750.

[50] L. You *et al.*, "Switching of perpendicularly polarized nanomagnets with spin orbit torque without an external magnetic field by engineering a tilted anisotropy," *Proc. Natl. Acad. Sci. U. S. A.*, vol. 112, no. 33, pp. 10310–10315, 2015, doi: 10.1073/pnas.1507474112.

[51] "OOMMF Project at NIST." https://math.nist.gov/oommf/.

[52] S. Fukami, T. Suzuki, H. Tanigawa, N. Ohshima, and N. Ishiwata, "Stack structure dependence of Co/Ni multilayer for current-induced domain wall motion," *Appl. Phys. Express*, vol. 3, no. 11, pp. 0–3, 2010, doi: 10.1143/APEX.3.113002.

[53] T. Komine, K. Takahashi, A. Ooba, and R. Sugita, "Reduction of intrinsic critical current density for current-induced domain wall motion by using a ferrimagnetic nanowire with perpendicular magnetic anisotropy," *J. Appl. Phys.*, vol. 109, no. 7, pp. 1–4, 2011, doi:

10.1063/1.3545797.

[54] S. Fukami, J. Ieda, and H. Ohno, "Thermal stability of a magnetic domain wall in nanowires," *Phys. Rev. B - Condens. Matter Mater. Phys.*, vol. 91, no. 23, pp. 1–7, 2015, doi: 10.1103/PhysRevB.91.235401.

[55] M. Arora, R. Hübner, D. Suess, B. Heinrich, and E. Girt, "Origin of perpendicular magnetic anisotropy in Co/Ni multilayers," *Phys. Rev. B*, vol. 96, no. 2, pp. 1–13, 2017, doi: 10.1103/PhysRevB.96.024401.

[56] N. R. Lee-Hone *et al.*, "Roughness-induced domain structure in perpendicular Co/Ni multilayers," *J. Magn. Magn. Mater.*, vol. 441, pp. 283–289, 2017, doi: 10.1016/j.jmmm.2017.05.051.

[57] J. M. Shaw, H. T. Nembach, and T. J. Silva, "Roughness induced magnetic inhomogeneity in Co/Ni multilayers: Ferromagnetic resonance and switching properties in nanostructures," *J. Appl. Phys.*, vol. 108, no. 9, 2010, doi: 10.1063/1.3506688.

[58] M. Arora *et al.*, "Magnetic properties of Co/Ni multilayer structures for use in STT-RAM," *J. Phys. D. Appl. Phys.*, vol. 50, no. 50, pp. 0–11, 2017, doi: 10.1088/1361-6463/aa97fa.

[59] L. Caretta *et al.*, "Fast current-driven domain walls and small skyrmions in a compensated ferrimagnet," *Nat. Nanotechnol.*, vol. 13, no. 12, pp. 1154–1160, 2018, doi: 10.1038/s41565-018-0255-3.

[60] K. J. Kim *et al.*, "Fast domain wall motion in the vicinity of the angular momentum compensation temperature of ferrimagnets," *Nat. Mater.*, vol. 16, no. 12, pp. 1187–1192, 2017, doi: 10.1038/nmat4990.

[61] S. A. Siddiqui, J. Han, J. T. Finley, C. A. Ross, and L. Liu, "Current-Induced Domain Wall Motion in a Compensated Ferrimagnet," *Phys. Rev. Lett.*, vol. 121, no. 5, p. 57701, 2018, doi: 10.1103/PhysRevLett.121.057701.

[62] K. Cai *et al.*, "Ultrafast and energy-efficient spin–orbit torque switching in compensated ferrimagnets," *Nat. Electron.*, vol. 3, no. 1, pp. 37–42, 2020, doi: 10.1038/s41928-019-0345-8.

[63] T. Shiino *et al.*, "Antiferromagnetic Domain Wall Motion Driven by Spin-Orbit Torques," *Phys. Rev. Lett.*, vol. 117, no. 8, pp. 1–6, 2016, doi: 10.1103/PhysRevLett.117.087203.

[64] O. Gomonay, T. Jungwirth, and J. Sinova, "High Antiferromagnetic Domain Wall Velocity Induced by Néel Spin-Orbit Torques," *Phys. Rev. Lett.*, vol. 117, no. 1, pp. 1–5, 2016, doi: 10.1103/PhysRevLett.117.017202.

[65] L. Sánchez-Tejerina, V. Puliafito, P. Khalili Amiri, M. Carpentieri, and G. Finocchio, "Dynamics of domain-wall motion driven by spin-orbit torque in antiferromagnets," *Phys. Rev. B*, vol. 101, no. 1, pp. 1–10, 2020, doi: 10.1103/PhysRevB.101.014433.